

See discussions, stats, and author profiles for this publication at: <https://www.researchgate.net/publication/283263490>

Tungsten Sulfide Quantum Dots as Multifunctional Nanotheranostics for in Vivo Dual-Modal Image-Guided Photothermal/Radiotherapy Synergistic Therapy

ARTICLE in ACS NANO · OCTOBER 2015

Impact Factor: 12.88 · DOI: 10.1021/acsnano.5b05825

READS

59

10 AUTHORS, INCLUDING:



Bao Tao

Chinese Academy of Sciences

4 PUBLICATIONS 2 CITATIONS

SEE PROFILE



Wenyan Yin

Chinese Academy of Sciences

46 PUBLICATIONS 986 CITATIONS

SEE PROFILE



Dongliang Wang

National Center for Nanoscience and Techn...

7 PUBLICATIONS 68 CITATIONS

SEE PROFILE



Zhanjun Gu

Chinese Academy of Sciences

82 PUBLICATIONS 2,105 CITATIONS

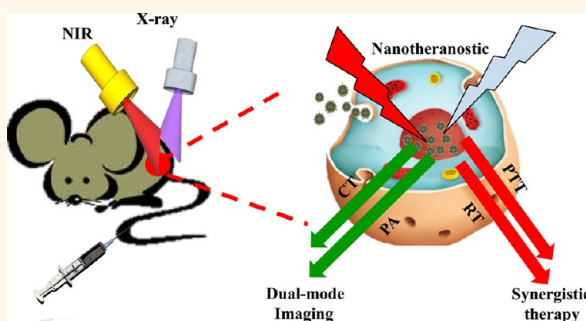
SEE PROFILE

Tungsten Sulfide Quantum Dots as Multifunctional Nanotheranostics for *In Vivo* Dual-Modal Image-Guided Photothermal/Radiotherapy Synergistic Therapy

Yuan Yong,[†] Xiaju Cheng,[‡] Tao Bao,[†] Mian Zu,[†] Liang Yan,[†] Wenyan Yin,[†] Cuicui Ge,[‡] Dongliang Wang,[†] Zhanjun Gu,^{*,†} and Yuliang Zhao^{*,†,‡}

[†]CAS Key Laboratory for Biomedical Effects of Nanomaterials and Nanosafety, Institute of High Energy Physics and National Center for Nanoscience Technology of China, Chinese Academy of Sciences, Beijing 100049, People's Republic of China and [‡]Collaborative Innovation Center of Radiation Medicine of Jiangsu Higher Education Institutions, and Jiangsu Provincial Key Lab of Radiation Medicine and Protection, School of Radiation Medicine and Protection, School for Radiological and Interdisciplinary Sciences, Soochow University, Suzhou 215123, People's Republic of China

ABSTRACT Designing a multifunctional nanomedicine for integration of precise diagnosis and effective treatment of tumors is desirable but remains a great challenge. Here, we report a multifunctional nanomedicine based on WS₂ quantum dots (QDs), which was prepared by a facile and “green” method through physical grinding and ultrasonication. The as-obtained WS₂ QDs with small size (3 nm) possess not only significant X-ray computed tomography (CT)/photoacoustic (PA) imaging signal enhancement but also remarkable photothermal therapy (PTT)/radiotherapy (RT) synergistic effect for tumor treatment. With CT/PA imaging and the synergistic effect between PTT and RT, the tumor could be accurately positioned and thoroughly eradicated *in vivo* after intravenous injection of WS₂ QDs. Moreover, hematoxylin and eosin staining, blood hematology, and biochemistry analysis revealed no noticeable toxicity of WS₂ QDs *in vitro* and *in vivo*, which confirmed that WS₂ QDs possess good biocompatibility. This multifunctional nanoparticle could play an important role in facilitating simultaneously multimodal imaging and synergistic therapy between PTT and RT to achieve better therapeutic efficacy.



KEYWORDS: WS₂ quantum dots · X-ray computed tomography · photoacoustic imaging · photothermal therapy · radiotherapy therapy · synergistic therapy

Photothermal therapy (PTT), which uses heat generated from absorbed near-infrared (NIR) light to ablate cancer, has received increasing attention due to its many advantages, such as low cost, highly localized and specific tumor treatment, fewer side effects, and minimal trauma to tissues.^{1–7} However, PTT alone always fails to eradicate tumors, especially for the deep-located tumors because of the inevitable depth-dependent decline of laser intensity, which is an intrinsic drawback of optical therapy. In view of this limitation, the combined therapy is usually considered as a very promising strategy to improve the therapeutic efficiency.^{8–12} Among various

therapies, radiation therapy (RT) is one of the most used treatments for cancer therapy in the clinic, which employs high-energy X-ray or γ -ray radiation to kill cancer cells with no depth restriction.^{13–15} However, RT suffers from low efficiency for killing the hypoxic cancer cells, which is believed to be one of the major causes for the failure of RT.^{16–19} Fortunately, PTT could efficiently kill the cancer cells that are not sensitive to RT. Moreover, an appropriate level of hyperthermia could increase intratumoral blood flow and subsequently improve oxygenation status in the tumor, which may cause the cells to be more sensitive to RT.^{20–22} Thus, combining PTT with RT is more

* Address correspondence to
zjgu@ihep.ac.cn,
zhaoyuliang@ihep.ac.cn.

Received for review September 16, 2015
and accepted October 23, 2015.

Published online
10.1021/acs.nano.5b05825

© XXXX American Chemical Society

preferable for enhanced therapeutic outcomes since it could take advantage of both and avoid the shortcomings of each. However, there is still a common problem that is faced in both PTT and RT. The high-energy X-ray radiation/light irradiation needed for tumor therapy may not only kill tumor cells but also exceed the tolerance of normal cells, leading to inevitable damage to normal tissues. Therefore, to address this challenge, the use of radiosensitizers/photothermal adsorbing agents to increase the local treatment efficacy under a relatively low and safe radiation/irradiation dose is highly desired.

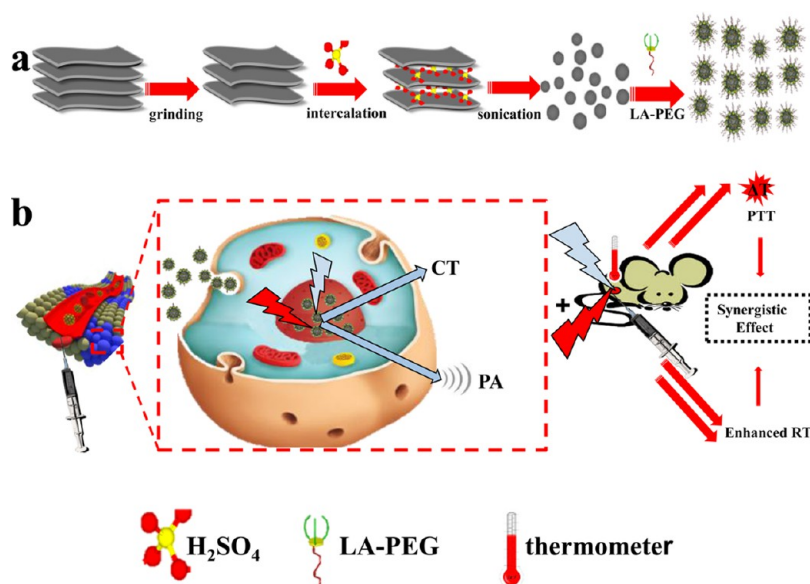
Recently, many nanomaterials have been employed as the photothermal adsorbing agents or radiosensitizers for enhancing the efficacy of PTT or RT, such as gold nanoparticles,^{23–28} CuS,^{29–34} Bi₂S₃,^{35,36} Bi₂Se₃,^{37,38} carbon-based nanomaterials,^{39–48} rare earth compounds,^{49–56} and so on. However, few of them could work for both PTT and RT at the same time to realize the combined therapy of PTT and RT. Moreover, most of the previously reported nanoparticles have relatively large diameters (typically >10 nm), which are above the threshold of kidney filtration. Consequently, these nanoparticles could not be excreted through the kidney and thus are trapped in the body for a long time period, which may have potential toxicity effects *in vivo* and thus hamper their clinical use. Therefore, there is still a great demand for developing a new nanomaterial that is ultrasmall but powerful to realize synergistic PTT/RT of tumors and to maximally avoid the side effects *in vivo*.

In this work, we fabricated WS₂ QDs and explored them as both radiosensitizers and photothermal adsorbing agents for combined PTT and RT, which has not been investigated to date. Nanoscaled transition metal dichalcogenides, such as MoS₂,^{57–61} and WS₂,^{62–66} have been used as new NIR absorbing agents for PTT ablation of cancer *in vitro* and *in vivo*. Moreover, due to its high Z number, WS₂ is anticipated to be a very competent candidate for use as radiosensitizers for enhanced PTT/RT synergistic therapy. The as-prepared WS₂ QDs with an average diameter of 3 nm could not only produce significant heat upon 808 nm laser irradiation but also simultaneously generate dose-enhancement effects of RT, resulting in remarkable *in vitro* cell damage and *in vivo* tumor regression. Compared to PTT or RT treatment alone, the combination of WS₂ QD-enhanced RT with PTT remarkably improved cancer cell killing and efficiently inhibited tumor growth, verifying the synergistic effect of the combination of PTT and RT. Furthermore, due to its high NIR absorption and strong X-ray attenuation, the WS₂ QDs could also be extended to use as a contrast agent for both X-ray computed tomography (CT) and photoacoustic (PA) imaging of tumors. As a result, the as-prepared WS₂ QDs offer a new possibility in exploring the ultrasmall but versatile nanoplatform for simultaneous biomedical imaging and combined RT and PTT of tumors.

RESULTS AND DISCUSSION

The WS₂ QDs were synthesized *via* a facile exfoliation method according to our previous report,^{62,67} which broke the weak van der Waals interaction forces between interlayers through physical grinding, H₂SO₄ intercalation, and ultrasonication (Scheme 1). With the increase of ultrasonication time, the size of the products could be gradually reduced to nanoscale, even a few nanometers, as illustrated in Figure 1a and Figures S1 and S2. For example, the as-obtained WS₂ nanoparticles with an average diameter of 3 ± 0.18 nm were fabricated by sonicating the sample for 3 h at a power output of 325 W (Figure 1b). This was further confirmed by atomic force microscopy (AFM), indicating the successful formation of WS₂ QDs (Figure 1c). X-ray diffraction (XRD) was employed to investigate the crystal phase and purity of the as-fabricated WS₂ QDs. The XRD result showed that all peaks correspond to the characteristics of hexagonal WS₂ (JCPDS card no. 08-0237), as shown in Figure 1d. No impurity peaks of any other phase were detected, confirming the high purity of the as-fabricated sample. In order to make them very dispersible in physiological solution and to improve their biocompatibility, a lipoic acid conjugated poly(ethylene glycol) (LA-PEG) was coated on the surface of the as-prepared WS₂ QDs through the formation of the W–S bond.⁶⁵ The IR spectra confirmed the successful coating of LA-PEG on the WS₂ QDs (Figure S3). The as-prepared PEG-WS₂ QDs exhibited good dispersibility in water and biofluids (Figure S4). The aqueous solution of PEG-WS₂ showed a brown color with a strong absorption in the UV to NIR region. Interestingly, with decreasing size, the absorption of WS₂ NPs was gradually enhanced, as illustrated in Figure 1e. The reason for this phenomenon may be that the smaller sizes of particles benefit their light harvesting by reducing the light transmittance and reflection that usually occurred in larger particles.^{68,69} Next, we evaluated the photothermal effect of WS₂ NPs with different sizes (Figure 1f). Correspondingly, the smaller NPs showed photothermal effects better than those of the larger ones. For example, the temperature of a solution containing WS₂ QDs (3 ± 0.18 nm, $100 \mu\text{g mL}^{-1}$) increased from 27 to 47 °C after NIR laser irradiation for 10 min (Figure 1f and Figure S5). The temperature of the larger NPs (~28 nm of diameter) only increased by ~12 °C under the similar experimental conditions. This result suggests that the smaller WS₂ QDs are more suitable for use as the PTT agent due to their better light-harvesting ability. The photothermal conversion efficiency (η value) of WS₂ QDs was also calculated to be 44.3% based on eq 1 (see Supporting Information for details).

$$\eta = \frac{hs(T - T_{\text{Surr}}) - Q_{\text{Dis}}}{I(1 - 10^{-A_{808}})} \quad (1)$$



Scheme 1. Schematic illustration of WS₂ QDs for dual-mode CT/PA imaging and PTT/RT synergistic therapy.

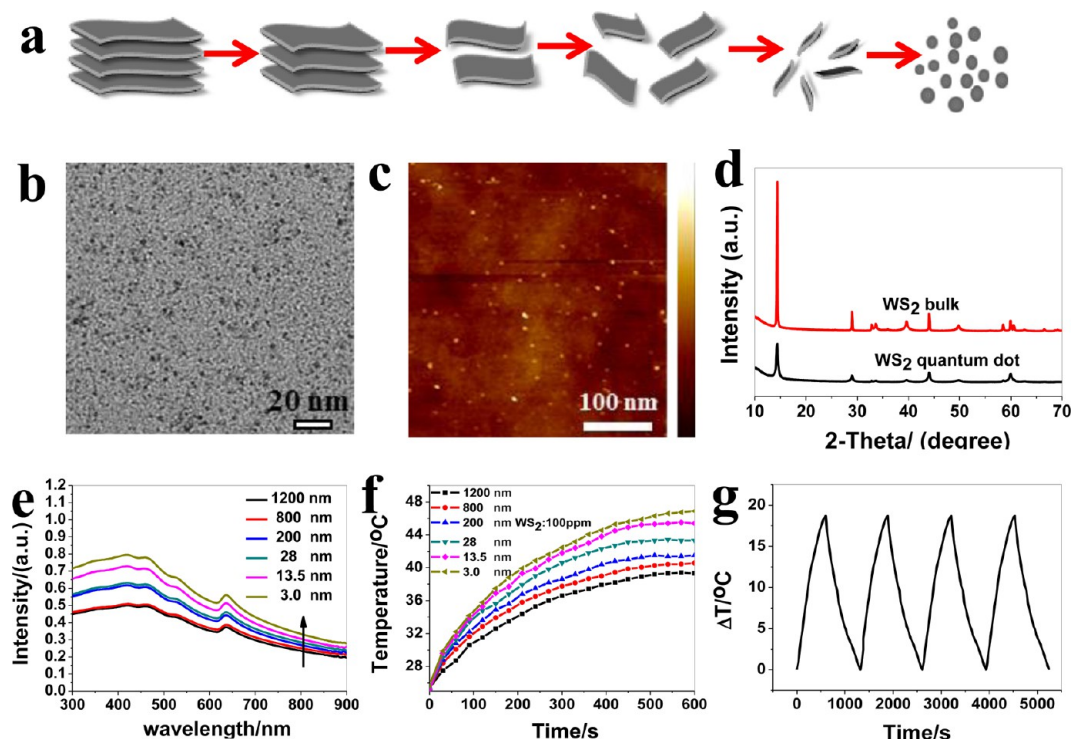


Figure 1. WS₂ QD characterization and photothermal effect of a WS₂ QD solution. (a) Synthetic process diagram of WS₂ nanoparticles with different sizes. (b) Transmission electron microscopy image of the as-made WS₂ QDs. (c) AFM topography images of the as-prepared WS₂ QDs. (d) XRD pattern of the as-synthesized WS₂ QDs. (e) UV-vis-NIR absorbance spectra of WS₂ particles with different sizes. (f) Temperature evaluation of WS₂ particles with different sizes. (g) Temperature change of WS₂ QD solution at a concentration of 100 ppm over four laser on/off cycles (1.0 W/cm²).

Moreover, the photostability of WS₂ QDs was measured by irradiating the sample with an 808 nm laser for 10 min and turning off the laser for four cycles (Figure 1g). We found that the temperature changes of WS₂ QDs had no obvious reduction, which implied that the WS₂ QDs had good photostability. All of these results suggest that the as-prepared WS₂ QDs have promising potential as PTT agents for cancer therapy.

Therefore, we chose the WS₂ QDs for further biomedical applications.

To meet the requirements of biomedical application, it is essential to examine the toxicity of WS₂ QDs. First, the standard cell counting kit 8 (CCK-8) assay and live/dead cell staining were carried out to evaluate the cytotoxicity of HeLa cells and HepG2 cells after they were incubated with WS₂ QDs for 24 h. No significant

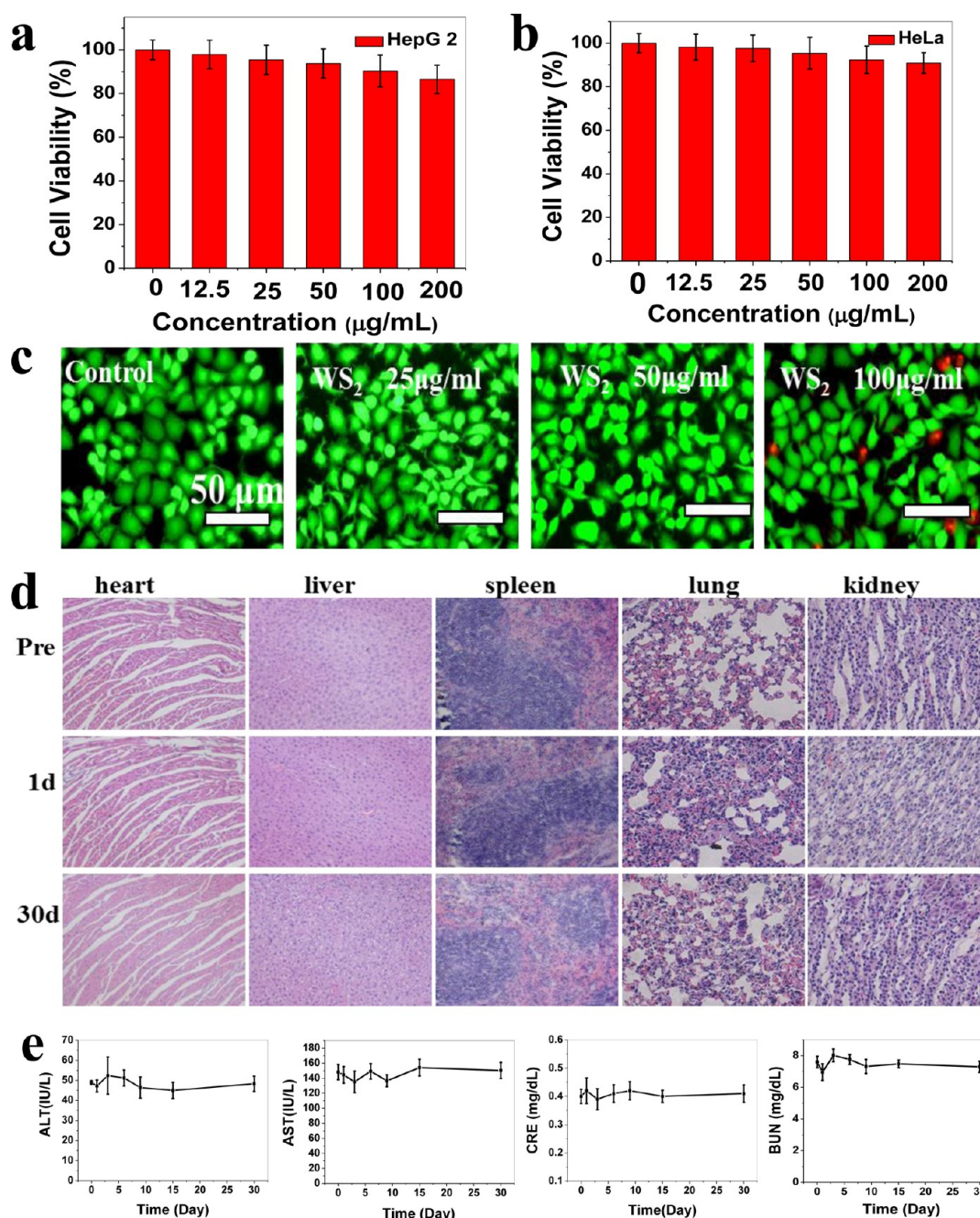


Figure 2. Toxicity experiments *in vitro* and *in vivo*. (a,b) Cell viability of HepG2 cells and HeLa cells after incubated with different concentrations of WS_2 QDs for 24 h. (c) Live–dead staining images of HeLa cells incubated with different concentrations of WS_2 QDs. (d) H&E stained images of organs of interest collected from mice after intravenous injection with WS_2 QDs (20 mg/kg). (e) Blood chemistry analysis of mice after being administered with WS_2 QDs (20 mg/kg). Hepatic function markers (ALT, AST) and renal function markers (CRE, BUN) were measured to be normal compared with the control group after 30 days, indicating no noticeable hepatic and renal dysfunction induced by WS_2 QDs. (ALT, alanine aminotransferase; AST, aspartate aminotransferase; CRE, creatinine; BUN, blood urea nitrogen).

cytotoxicity of WS_2 QDs was observed in both cells, even at a high concentration up to $200 \mu\text{g mL}^{-1}$, where the cell viabilities of HeLa and HepG2 cells are still higher than 85% (Figure 2a,b). This was visually confirmed further by live/dead cell staining, as shown in Figure 2c, indicating the low cytotoxicity of WS_2 QDs. *In vivo* experiments including body weight, biodistribution, hematoxylin and eosin (H&E) staining, and blood biochemistry analysis were also conducted to ensure

the safe application of WS_2 QDs *in vivo*. The results indicate no obvious signs of abnormal mouse behavior in body weight, eating, drinking, and activity. The H&E staining showed no obvious tissue damage in the main organs (Figure 2d), and significant parameters of blood hematology and biochemistry analysis also indicated no noticeable changes, in contrast with that of the control group (Figure 2e). The biodistribution results reported that QDs were mainly accumulated in the

kidney, liver, and spleen (Figure S6). However, hepatic function markers (ALT, AST) and renal function markers (CRE, BUN) were measured to be normal after 30 days the treatment with WS₂ QDs, indicating no noticeable hepatic and renal dysfunction induced by WS₂ QDs (Figure S7 and Table S1). After 30 days, most of the WS₂ QDs were excreted from the body. These preliminary results proved that WS₂ QDs have low toxicity to mice at least at our tested dose. The reason for the lower toxicity of our obtained WS₂ QDs may be that we prepared these WS₂ QDs by mainly physical grinding and ultrasonication without using any toxic organic solvents and chemicals. Therefore, the strategy presented in this work is very “green” for the fabrication of WS₂ QDs with low toxicity. In addition, the small size of as-prepared WS₂ QDs facilitated its clearance from the body, which may reduce the concern for their long-term toxicity and thus benefit their use in further bioapplications.

The low toxicity of WS₂ QDs and its high NIR/X-ray absorption ability encouraged us to evaluate their potential as photothermal agents and radiosensitizers for synergistic PTT and RT of cancer cells. Clonogenic assay was conducted to assess the cell viability in 4T1 cells after the different treatments. As depicted in Figure 3a,b, NIR alone and X-ray alone treatment decreased 4T1 cell colony formation to 97 and 75%, respectively, while NIR + WS₂ and RT + WS₂ drastically inhibited cell survival to 39 and 31%, indicating that WS₂ QDs have great potential for use as both photothermal agents and radiosensitizers. Next, we evaluated the synergistic effect caused by WS₂-enhanced RT/PTT combinational therapy. It was found that cell viability substantially decreased to 6%, which was 80.6% lower than that of WS₂-enhanced RT alone and was 84.6% lower than that of WS₂-enhanced PTT alone, confirming the considerable WS₂-enhanced RT/PTT synergistic effect *in vitro*. Moreover, as shown in Figure 3c, obvious enhancement in RT with increasing radiation dose was observed for the cells treated with WS₂ QDs and WS₂ QDs + NIR. The radiation enhancement is usually considered to be caused by DNA damage induced by the photoelectric effect and Compton scattering of the high Z element (W atom). This hypothesis was confirmed by a DNA staining method (γ -H2AX staining) (Figure 3d). This assay analyzed the double DNA strand break, which correlates to the overall absorbed radiation dose. It was found that the number of γ -H2AX foci/100 μm^2 (shown as red fluorescent spots) was enhanced by 1.5 and 2.1 times for the cells treated with WS₂ QDs and WS₂ QDs + NIR, respectively, compared with radiation alone (Figure 3e). The sensitizer enhancement ratio (SER), which is a measure of how effectively a radiosensitizer reduces tumor cell proliferation, was also calculated and is displayed in Figure 3f (see experimental section in the Supporting Information). The SER

for a WS₂ QD dose of 100 $\mu\text{g/mL}$ was about 1.22, and this value increased to 1.31 when combined with NIR treatment, further confirming the PTT-enhanced RT of cancer cells. These results further demonstrated the induction of apoptosis by WS₂ QD-enhanced PTT/RT of cancer cells.

Motivated by the effective synergistic RT/PTT efficacy *in vitro*, we further investigated the feasibility of WS₂ QDs as the photothermal agent and radiosensitizer for RT/PTT synergistic therapy *in vivo* by intratumoral administration. When the tumor volume reached approximately 75 mm³, 28 BEL-7402 tumor-bearing BALB/c nude mice were divided into seven groups to receive different disposes: (a) PBS (phosphate buffered saline) only; (b) WS₂ QDs only; (c) NIR only; (d) RT only; (e) WS₂ QDs + RT; (f) WS₂ QDs + NIR; (g) WS₂ QDs + NIR + RT. Next, the relative tumor volume change and body weight of all of these groups were recorded as a functional of time (Figure 4c,d and Figure S8 in the Supporting Information). As shown in Figure 4, at 22 days after treatment, tumors in groups a, b, and c grew rapidly with relative tumor volume (V/V_0) of 24.03 ± 3.09 , 22.78 ± 2.47 , and 22.77 ± 1.60 , respectively, which indicated that the single employment of WS₂ QDs or 808 nm laser (1 W/cm^2) had negligible effects on tumor growth (Table S2), while the mice treated with both NIR and WS₂ QDs exhibited efficient tumor growth inhibition (TGI) of 86.11% ($V/V_0 = 3.338 \pm 0.93$) after 22 days (Figure 4e). The IR thermal camera revealed that the temperature of the tumor area increased remarkably to $\sim 45^\circ\text{C}$ after being irradiated with an 808 nm laser (power density: 1.0 W/cm^2) for 10 min, which was capable of killing cancer cells by moderate hyperthermia and restricting its malignant proliferation (Figure 4a,b). In the contrast, the tumor temperatures of mice injected with PBS only increased by $\sim 3^\circ\text{C}$, indicating the promising potential of WS₂ QDs as an efficient PTT agent for photothermal ablation of tumors. Similarly, the mice treated with RT alone and RT + WS₂ QDs also showed obvious tumor growth delay. Compared to RT along (group d, $\text{TGI} = 37.64\%$, $V/V_0 = 14.985$), the integration of WS₂ QDs and RT (group e, $\text{TGI} = 56.85\%$, $V/V_0 = 10.37$) showed more effective inhibition of tumor growth, indicating the efficient sensitization effect of WS₂ QDs on RT. The most efficient tumor growth delay was achieved by the treatment of WS₂ QDs + NIR + RT. As shown in Figure 4f–h, the mean tumor weight and tumor photograph in group g exhibited thorough elimination 5 days after treatment without recurrence during the next following 17 days, demonstrating the obvious WS₂ QD-enhanced RT/PTT synergistic therapy in contrast with that of WS₂ + NIR or WS₂ + RT alone. This was also confirmed by the pathological test with H&E staining (Figure 4i). The H&E staining images of a tumor slice collected at 22 days after the treatment revealed that most tumor cells were destroyed after the RT/PTT combinational therapy, while

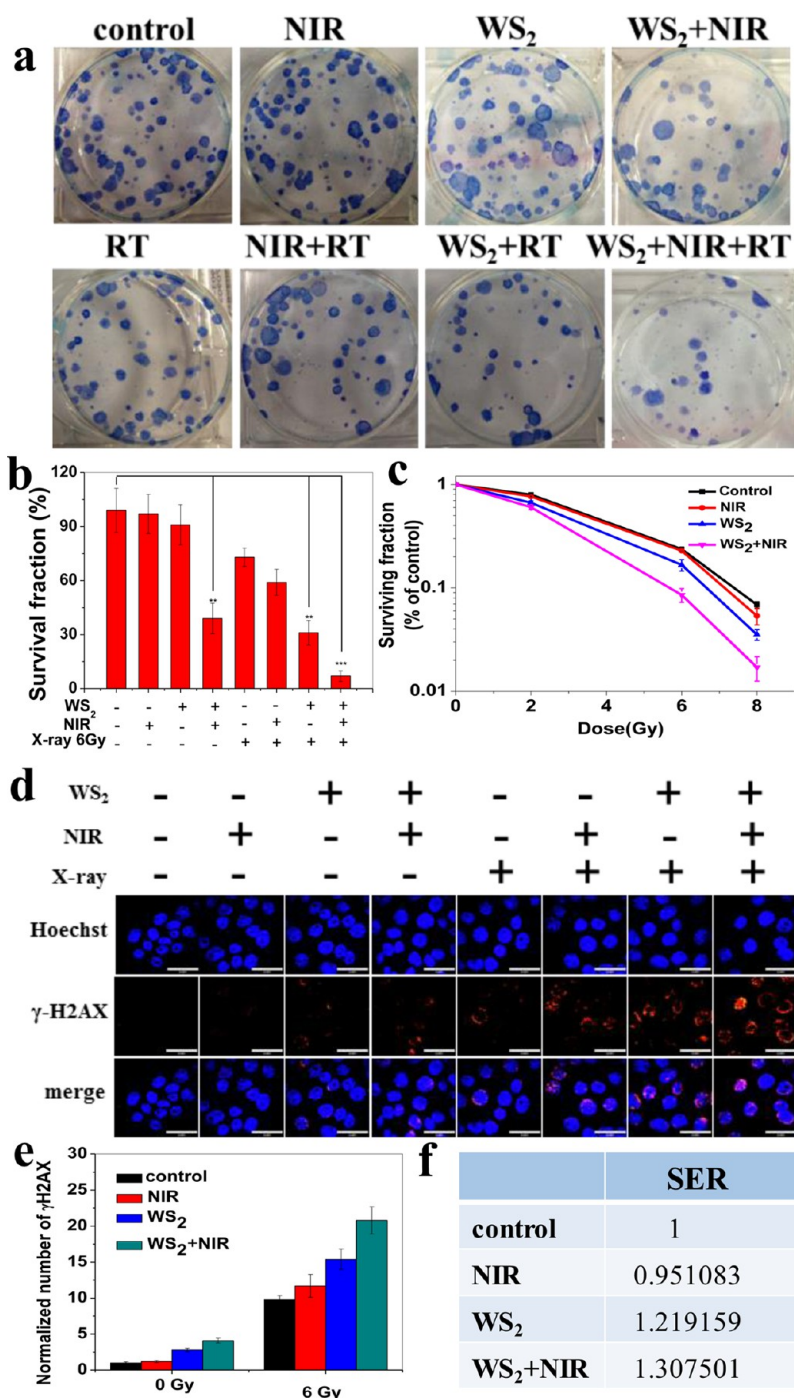


Figure 3. WS₂-enhanced photothermal therapy and radiotherapy increased apoptosis in 4T1 cells. (a) Colony of 4T1 cells treated with WS₂ QDs (100 ppm, 2 mL) combined with 808 laser lamp irradiation (1 W/cm², 10 min) and X-ray radiation (6 Gy). (b) Responding survival fraction of 4T1 cells with different treatments. (c) WS₂ QDs in combination photothermal therapy and X-ray radiation decreased 4T1 cell survival detected by clonogenic assay. (d) Representative fluorescence images of DNA fragmentation and nuclear condensation induced by WS₂ QDs (100 ppm, 2 mL) and/or 808 nm laser lamp (1 W/cm², 10 min) and/or X-ray radiation (6 Gy), stained with Hoechst and γ -H2AX for nuclear visualization and DNA fragmentation, respectively. (e) Corresponding normalized number of γ -H2AX after WS₂ QDs (100 ppm, 2 mL) and/or 808 nm laser lamp (1 W/cm², 10 min) and/or X-ray irradiation (6 Gy). (f) Sensitizer enhancement ratio of WS₂, NIR, and WS₂ + NIR. Error bars were based on standard deviation of four parallel samples. *P* values were calculated by the student's test: ***P* < 0.01, ****P* < 0.001.

the monotherapy only induced partial damage on tumor tissues, further demonstrating the distinct WS₂ QD-enhanced RT/PTT synergistic effects. This enhancement may be attributed to the sensitization effect of mild temperature elevation with radiotherapy since the

WS₂ QD-mediated photothermal therapy could not only damage some radio-resistant hypoxic cells and the superficial cancer cells but also change the oxygenation environment of the remaining cells, leaving them relatively radio-sensitive and easily killed by RT. In this case,

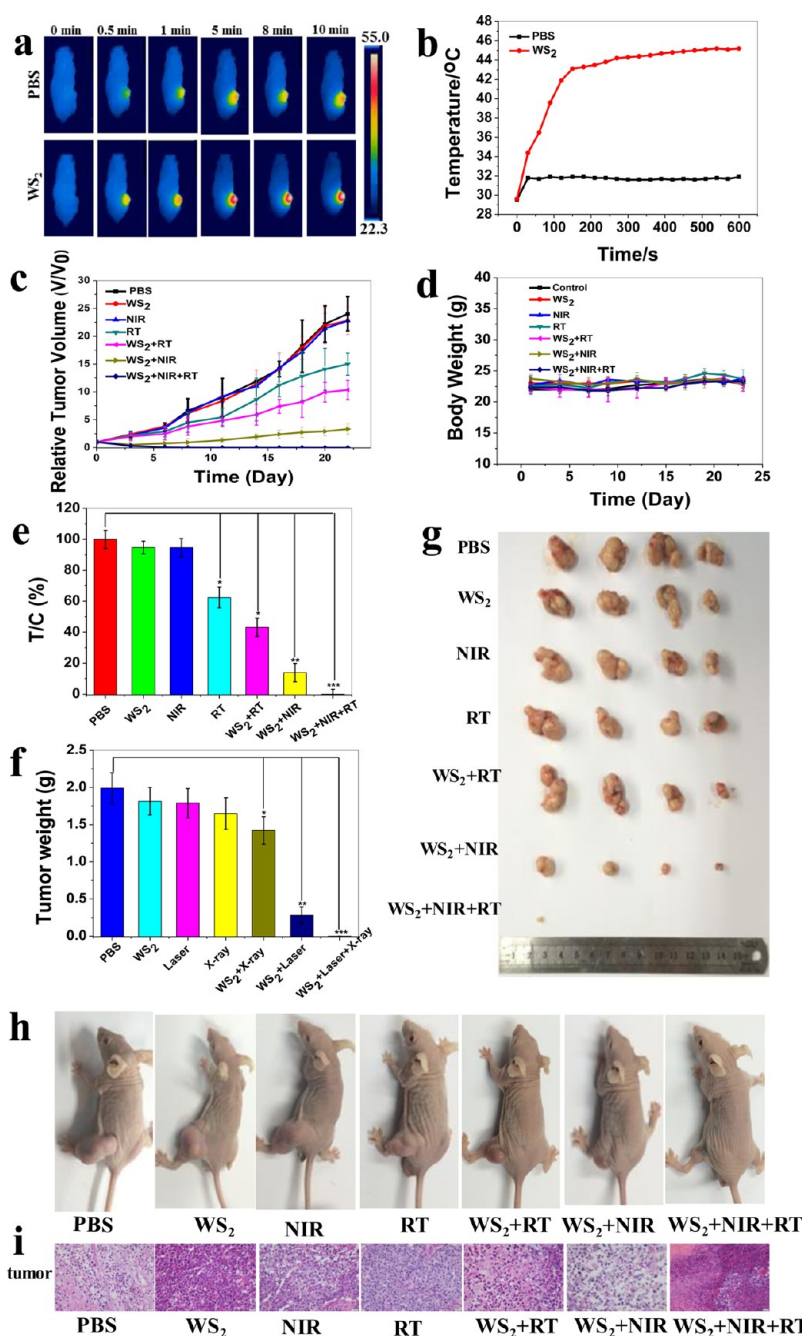


Figure 4. *In vivo* WS₂ QD-enhanced RT/PTT synergistic therapy of tumor-bearing mice. (a,b) Photothermal images and temperature plot of BEL-7402 tumor-bearing mice with i.t. administration of a WS₂ QD solution (2 mg/mL, 20 μ L) irradiated with an 808 nm laser at a power density of 1 W/cm² for 10 min. PBS was used as the negative control group. (c) Relative tumor volume profiles of different groups of mice after different administration: (i) PBS injection; (ii) WS₂ QDs i.t. injection; (iii) laser only; (iv) X-ray only; (v) WS₂ QDs + X-ray; (vi) WS₂ QDs + laser; (vii) WS₂ QDs + laser + X-ray. (d) Body weight of different groups of BEL-7402 tumor-bearing mice after various treatments. (e) Tumor inhibition rate of different groups of BEL-7402 tumor-bearing mice. (f) Average weight of tumors collected from each group of tumor-bearing mice after photothermal therapy and radiotherapy. (g) Photos of tumors collected from each group of the BEL-7402 tumor-bearing mice after various treatments. (h) Representative images of different groups of BEL-7402 tumor-bearing mice after different administrations at the end of photothermal therapy and radiotherapy. (i) H&E stained images of tumors collected from different groups of mice. Error bars were based on standard deviation of at least four parallel samples. *P* values were calculated by the student's test: **P* < 0.05, ***P* < 0.01, ****P* < 0.001 (*n* = 4 per group).

our results demonstrated that WS₂ QDs have potential as a promising agent for PTT-enhanced RT tumor eradication and effectively prevent their recovery.

Ideal nanoparticle systems in nanomedicine should possess multimodality in both imaging and therapy.

Precise spatial- and temporal-specific monitoring of PTT agents and radiosensitizers *in vivo* is particularly demanded as it potentially opens a novel avenue in guiding the therapeutic process, monitoring the therapeutic response, and avoiding the destruction

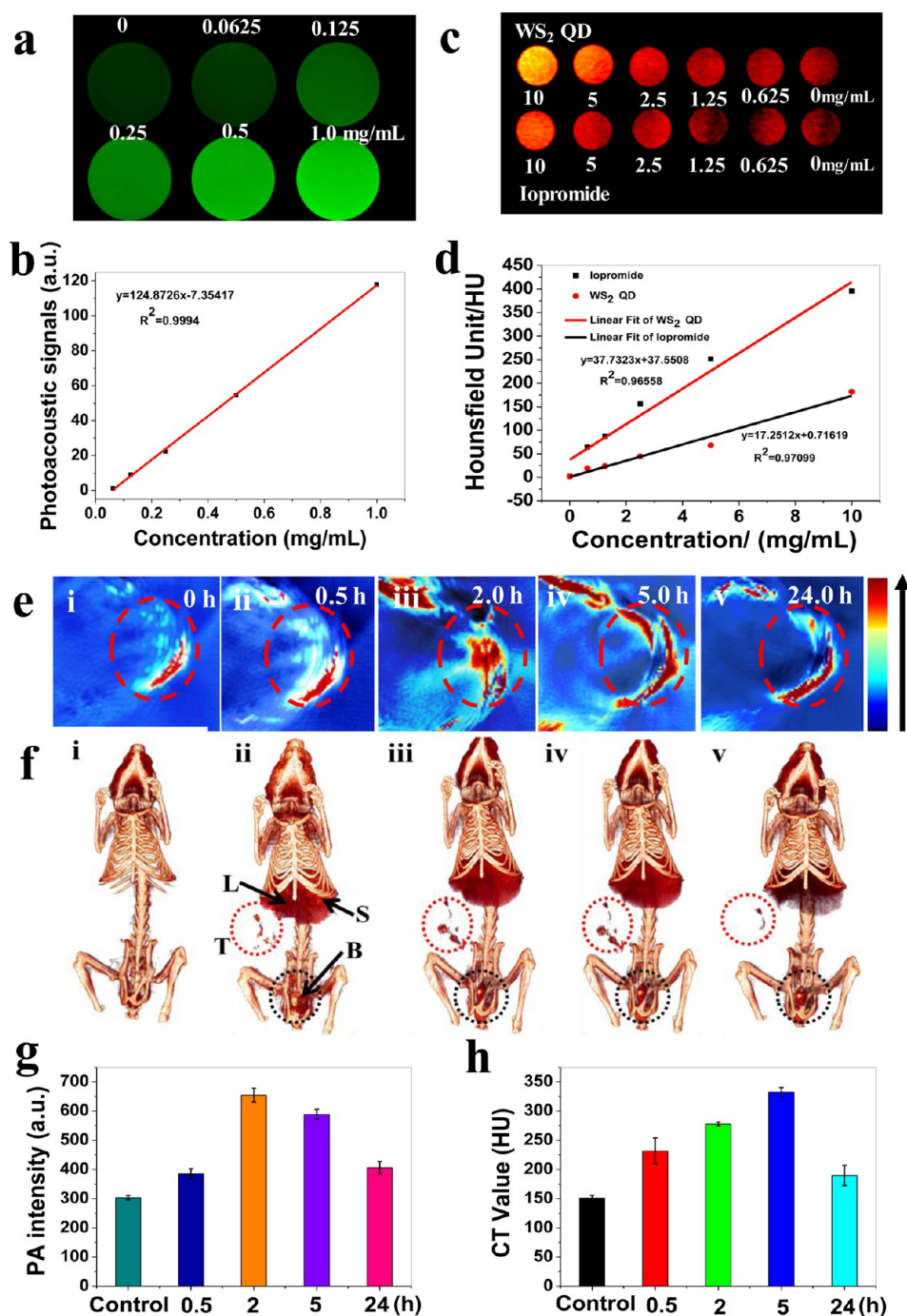


Figure 5. CT and PA imaging *in vitro* and *in vivo*. (a) *In vitro* PA images of WS₂ QD solution with different concentrations. (b) Photoacoustic signal of aqueous WS₂ QDs as a function of the WS₂ QD concentration, based on results from c. (c) X-ray CT images *in vitro* of commercially used iopromide and WS₂ QD samples with different concentrations. (d) Hounsfield unit values of iopromide and WS₂ QD samples as the function of their corresponding concentrations, where the slope of the profiles was 17.2513 and 37.7323, respectively. (e) PA images of BEL-7402 tumor-bearing mice before and after i.v. administration of WS₂ QD solution (2 mg/mL, 200 μ L) at different time points (0.5, 2, 5, and 24 h). (f) CT images of tumor before and after i.v. administration of WS₂ QD solution (15 mg/mL, 200 μ L) at different time points (0.5, 1, 2, and 24 h). (g) Corresponding intensity of the photoacoustic signal of WS₂ QDs in the tumor at different time points. (h) Corresponding HU value of WS₂ QDs in the tumor at different time points.

induced by external radiation to surrounding healthy tissue, which consequently would reduce the associated side effects. Due to their high NIR absorption and strong X-ray attenuation ability, the WS₂ QDs are anticipated to be qualified for both X-ray CT and PA

imaging of tumors. PA is a new technology based on the photoacoustic effect of light absorbers, and thus WS₂ QDs appeared to be a desired contrast agent for PA imaging.⁶⁵ PA is greatly welcomed for cross-sectional "listening" of entire tumors at depths not

available to microscopy and sensitivity not available to CT imaging. As expected, the photoacoustic signal of WS₂ QDs greatly enhanced with the increase of WS₂ QD concentrations (Figure 5a,b) and correlated linearly with WS₂ QD concentrations, indicating that WS₂ QDs should be a promising candidate for PA imaging. Next, we used the PA signal to monitor the accumulation of WS₂ QDs *in vivo* (Figure 5e). WS₂ QDs (200 μ L, 2 mg/mL) were intravenously injected into the tail vein of BEL-7402 tumor-bearing BALB/c nude mice, and then the cross-sectional PA signal of tumors was obtained at different times. Before WS₂ QD injection, the PA image showed observable but weak PA signals in the tumor region, which arise from the tumor blood, while PA signals remarkably increased after i.v. injection, indicating the gradual accumulation of WS₂ QDs in tumor sites. After administration of WS₂ QDs for 2 h, the PA signal reached \sim 655 au, which was 2 times higher than that before injection (\sim 304 au) in the tumor and lasted as long as 24 h (Figure 5g). This result clearly demonstrated that WS₂ QDs could efficiently and passively target the tumor site and stay there for a long time. The PEG coating and appropriate particles size may contribute to its significant passive targeting and long residence time in tumors. In addition, considering the high atomic number and X-ray absorption coefficient of the tungsten, these WS₂ QDs could also be used as CT imaging contrast agents in CT imaging, which is one of the most commonly used imaging tools for medical diagnosis and can afford high-resolution 3D structural details of the whole body. The combination of PA and CT imaging could offer whole-body imaging with high spatial resolution without depth limitation and thus allow better understanding of the subtle changes in tumors.^{65,66} To examine their CT contrast performance *in vitro*, different concentrations of WS₂ QDs dispersed in 0.5% agarose gel solution and the same concentrations of iopromide (a commercial iodine-based CT contrast agent in the clinic) were used as the control group. As shown in Figure 5c,d, the CT signal of WS₂ QDs dispersed in 0.5% agarose gel was concentration-dependent. With the increase of WS₂ QD concentration, the signal intensity of WS₂ QDs was sharply enhanced. The Hounsfield units (HU) value of WS₂ QDs was about 37.23 HU L/g, which was 2 times higher than that of iopromide (17.2512 HU L/g) at the same concentration, indicating the good contrast efficacy of WS₂ QDs for CT imaging. This enhancement of the X-ray attenuation possibly results from the fact that

W has an X-ray absorption efficiency higher than that of iopromide (4.438 and 1.194 cm²/g for W and I at 100 keV, respectively).^{37,70} Encouraged by its good performance *in vitro*, we next pursued the application of WS₂ QDs used as CT contrast agents *in vivo* (Figure 5f). BEL-7402 tumor-bearing BALB/c nude mice were intravenously administrated with 200 μ L of WS₂ QD samples (15 mg/mL) and then imaged on the small mice X-ray CT at different times (0.5, 1.0, 2.0, and 24 h) after injections. The obtained images at different time points revealed obvious enhanced contrast in the tumor with the HU value increased from 151.3 ± 4.2 before injection to 332.7 ± 27.4 after i.v. administration of WS₂ QDs (Figure 5h). After 2.0 h post-WS₂ QD injection, Figure 5 showed remarkable CT contrast signals in tumors, which confirms the sufficient accumulation of WS₂ QDs in tumors. This tumor-homing effect as shown in the CT imaging is in agreement with the PA results. Thus, WS₂ QDs have remarkable PA/CT imaging capabilities and obvious tumor-homing effects. In addition, obvious enhanced contrast in liver and spleen was observed after i.v. injection of WS₂ QDs, which demonstrated the accumulation of WS₂ QDs by the reticuloendothelial system. Moreover, high contrast enhancement was also found in the bladder, suggesting that WS₂ QDs with ultrasizes in the range of 2–3 nm might be cleared out through renal excretions, which greatly enhances its clearance out of the body and thus minimizes the potential side effects of WS₂ QDs.

CONCLUSION

In summary, multifunctional nanotheranostics based on WS₂ QDs only without any other component has been successfully fabricated to achieve simultaneous CT/PA imaging and synergistic PTT and RT treatment of tumors. The as-fabricated WS₂ QDs exhibited good CT/PA imaging capacity and remarkable PTT/RT synergistic effect, which favors the precise positioning of the location of the tumor and realizing the eradication of the tumor. Moreover, no noticeable toxicity of WS₂ QDs was observed *in vitro* and *in vivo*, which confirmed that WS₂ QDs possess good biocompatibility. Our results not only promise the use of WS₂ QDs as a small yet powerful platform for the multimodal image-guided PTT/RT synergistic therapy but also encourage further exploration of other radio-sensitization-based multifunctional nanotheranostics for cancer diagnosis and therapy.

EXPERIMENTAL SECTION

Materials. All chemicals and reagents were used as received without any further purification. Commercial bulk tungsten disulfide (WS₂, 99.8%) was purchased from Alfa Aesar Company, and sulfuric acid (H₂SO₄, 95.0%, \sim 98.0%) was supplied by

Beijing Chemical Corporation. Polyethylene glycol and lipoic acid were obtained from Alfa Aesar Company. CCK-8 and calcein-AM (CA)—propidium iodide (PI) stain were both purchased from Dojindo Laboratories in Japan. γ -H2AX antibody was supplied by Abcam Company. Cy3 antibody and Hoechst were obtained from Beyotime Biotechnology. PE annexin

V apoptosis detection kit was purchased from BD. Dulbecco's modified Eagle medium (DMEM) and fetal bovine serum (FBS) were purchased from Gibco Company. Deionized (DI) water was used throughout. Male BALB/c mice were purchased from Weitong Lihua Experimental Animal Technology Co. Ltd.

Preparation of WS₂ Quantum Dots. WS₂ QDs were synthesized according to the previously reported method.⁶² Briefly, commercial WS₂ bulk was ground by a grinding miller for about 3–4 h. Next, 60 mg of ground WS₂ powder was dispersed in about 60 mL of H₂SO₄ (95.0%, ~98.0%) at 90 °C for 1D intercalation. Following the intercalation by H₂SO₄ (95.0%, ~98.0%), the intercalated WS₂ sample was centrifuged and washed repeatedly with DI water to remove excess sulfuric acid. Subsequently, the intercalated WS₂ sample was dispersed in 30 mL of DI water for further ultrasonication for 3 h to obtain a WS₂ solution, which was centrifuged in 12 000 rpm to obtain the WS₂ QDs. The as-synthesized WS₂ QD precipitation was redispersed in pure water and stored at 4 °C for future experiments. The yield of the as-prepared WS₂ QDs is calculated to be 72% based on W atoms. Similarly, WS₂ nanoparticles with different sizes were also fabricated by varying the ultrasonication time (0.5, 1, 1.5, 2, 2.5 h) while keeping other conditions unchanged.

PEGylation of WS₂ Quantum Dots. Lipic acid-modified PEG (LA-PEG) was prepared as described in the previously reported protocol.⁶⁵ Briefly, 45 mg of LA was mixed with 500 mg of 5 km PEG-NH₂ (mPEG-NH₂/LA molar ratio = 1:2) dissolved in 2 mL of dichloromethane for 1 day in the presence of 6 μ L of triethylamine and 10 mg of *N,N'*-dicyclohexylcarbodiimide (Alfa Aesar Company). After being blown with nitrogen, some solid in the bottle was yielded, and then 10 mL of pure water was added. To remove the insoluble solid, the yielding solution was filtered. Subsequently, sodium bicarbonate was added to adjust the pH value of the solution to 8.0, and the filtration solution was then extracted with dichloromethane four times. After the organic solvent was removed, the sample was dissolved in water and lyophilized. Finally, LA-PEG was synthesized. To make the synthesized WS₂ QDs more water-soluble, the as-made LA-PEG was coated on the surface of WS₂ QDs. In a typical synthesis, 20 mg of LA-PEG was added into 2 mL of WS₂ QDs (1 mg/mL) by sonication for 30 min and stirring for 10 h at room temperature. The as-prepared WS₂-PEG was highly water-soluble and stored at 4 °C for further experiment.

Photothermal Evaluation of WS₂ QDs. To assess the photothermal effect of the as-synthesized WS₂ QD samples, various concentrations of WS₂ QD samples were irradiated under an 808 nm laser at a power density of 1 W/cm² for 10 min. An IR thermal camera was used to record the temperature of the solution at each time point. Meanwhile, an 808 nm NIR laser with different power densities (1.0, 0.8, 0.5, 0.3 W/cm²) was also used to irradiate the WS₂ QDs (100 μ g/mL) for 10 min and the other experimental conditions kept the same. To evaluate the NIR stability of WS₂ QDs, 100 μ g/mL of WS₂ QDs was irradiated for 10 min at a power density of 1 W/cm² and then the laser was turned off. This procedure was repeated four times to assess its photostability.

Cytotoxicity Evaluation and Photothermal Therapy *in Vitro*. HeLa in DMEM (high glucose) and HepG2 cells maintained in improved minimum essential medium supplemented with 10% fetal bovine serum (GIBCO) at 37 °C under a humidified atmosphere with 5% CO₂. The cell viability was assessed by the CCK-8 method. The cells were cultured in a 96-well culture plate at a density of 3×10^4 per well. After being incubated for 24 h, different concentrations of WS₂ QDs were added to co-incubate with the cells for 24 h. Next, 10 μ L of CCK-8 was added and further cultured for 2 h at 37 °C. After incubation, the CCK-8 test was performed immediately after treatment of the cells. The microplate reader (Thermo Scientific, MULTISCAN MNK3) was used to measure the absorbance of the samples at the characteristic peak of 450 nm. To test the PTT effect *in vitro*, human cervical cancer cells maintained in DMEM (high glucose) supplemented with 10% FBS (GIBCO) was cultured in 6-well plates at a density of 4×10^4 per well for 24 h. After the cells had grown to the full bottom of the plates, the cells were set to four groups (control, laser only, WS₂ QDs, WS₂ QDs + laser). The first group had no dispose. The second group was irradiated with an

808 nm laser with a different power density (0.3, 0.5, 1.0 W/cm²) for 10 min. The third group was cultured with different concentrations of WS₂ QDs (25, 50, and 100 μ g/mL) for 24 h and simultaneously irradiated with different power densities (0.3, 0.5, 1.0 W/cm²) for 10 min. After treatment, the cells were further cultured for 12 h at 37 °C under a humidified atmosphere with 5% CO₂ without light interference. The culture medium was washed several times with PBS and stained with CA-PI for 15 min. After being stained and washed twice again with PBS, an inverted luminescence microscopy (OLYMPUS X73, Japan) was applied to take the luminescence images.

Clonogenic Assays. 4T1 cells were incubated in 6-well plates at different numbers (100, 200, 300, 600, 1000 cells) and allowed to attach for 48 h. The cells were treated with 100 μ g/mL WS₂ QDs for 24 h, respectively. After 24 h incubation, the cells were treated with or without the 808 nm laser and X-ray irradiation. The plates with different numbers of cells were treated with different doses of radiation (0, 2, 6, and 8 Gy). Next, the cells were further incubated for another 10 days. Finally, colonies were stained with Giemsa dye, and the survival fraction of the colonies was used to evaluate the effects of different treatments.

DNA Double-Strand Breaks. 4T1 cells were maintained in a 35 mm confocal dish at a density of 2×10^4 per well for 24 h and divided into eight groups (control, WS₂ QDs, NIR, and WS₂ QDs + NIR with or without X-ray irradiation). When 4T1 cells had grown to 30% in plates, 2 mL of WS₂ QDs (100 μ g/mL) was added and further cultured for 24 h. The well without any treatments was regarded as the negative control group. After 24 h incubation, cells were irradiated with or without an 808 nm laser (1 W/cm², 10 min) and X-ray (6 Gy). The synergistic treatment group was irradiated with X-rays immediately after irradiation with an 808 nm laser. After 24 h, the cells were fixed with 4% paraformaldehyde for 10 min and Triton X-100 was used to permeate the cells. Next, the cells were further incubated in 1% bovine serum albumin for another 1 h to prevent nonspecific protein interactions. Next, the cells were then treated with γ -H2AX antibody (ab81299, Abcam Inc.) overnight at 4 °C. The secondary antibody Cy3 tag goat anti-rabbit IgG (H+L) was added for 1 h. Hoechst was used to stain the cell nuclei.

CT and PA Imaging *in Vitro*. To test the linearity of the CT signal as a function of WS₂ QD concentration, various concentrations of WS₂ QDs were dissolved in the 0.5% agarose gel solution and then set in the 1.5 mL centrifuge tubes for *in vitro* CT signal detection. For comparison, the same concentrations of iopromide (Ultravist300, Bayer) were used as the control group. The Gamma Medica-Ideas instrument was employed to accomplish CT imaging, and the Triumph TM X-O TM CT system was further used to obtain the Hounsfield unit values and CT images. The following imaging parameters were used: effective pixel size, 80 kV, 50 μ m, 270 μ A; field of view, 1024 pixels \times 1024 pixels. Meanwhile, to evaluate the linearity of the PA signal as a function of WS₂ QD concentration, different concentrations of WS₂ QDs dissolved in purified water were used for *in vitro* PA signal detection.

CT and PA Imaging *in Vivo*. For PA imaging *in vivo*, BEL-7402 tumor-bearing BALB/c nude mice were intravenously injected with 200 μ L of WS₂ QD samples (2 mg/mL). After the injection, the signal was recorded on the PA instrument (MSOT invasion 128, iTheramedical, Germany) at different time points (0.5, 2, 5, and 24 h). The PA signal before injection was used as the control. Different wavelengths (700–900 nm) of excitation light were used to collect the photoacoustic signals. Imaging parameters were as follows: the region of interest is 20 mm, and the 10 wavelengths for each slice were from 700 to 900 nm. For CT imaging *in vivo*, 200 μ L of WS₂ QD samples (15 mg/mL) was i.v. injected into the tail vein of BEL-7402 tumor-bearing BALB/c nude mice. Next, the mouse was set on a small X-ray CT (Gamma Medica-Ideas) to image at different time intervals (0.5, 1, 2, and 24 h). To obtain reconstruction images, the filtrated back projection method was carried out to reconstruct images, and the Amira 4.1.2 system was used to analyze the reconstruction images. The main parameters were as follows: tube voltage 80 kV, effective pixel size 50 μ m, tube current 270 μ A; field of view, 1024 pixels \times 1024 pixels.

PTT/RT Synergistic Therapy *in Vivo*. All animals were maintained under protocols approved by the Key Laboratory for Biomedical Effects of Nanomaterials and Nanosafety (Institute of High Energy Physics, CAS). The left hind legs of 28 BALB/c male mice were subcutaneously implanted with 1.0×10^6 BEL-7402 cells suspended in 100 μ L of PBS. When the tumor volume reached approximately 75 mm³, the mice were divided into seven groups and each group included four mice: (a) PBS only; (b) WS₂ QDs only; (c) NIR only; (d) RT only; (e) WS₂ QDs + RT; (f) WS₂ QDs + NIR; (g) WS₂ QDs + NIR + RT. The BEL-7402 tumor-bearing BALB/c nude mice in groups b, e, f, and g were intratumorally injected with 20 μ L of WS₂ QDs (2 mg/mL). After 1.5 h, the BEL-7402 tumor-bearing BALB/c nude mice in group f were exposed to an 808 nm laser at a power density of 1 W/cm² for 10 min in the tumor site, and a NIR camera was simultaneously used to record the temperature change of the tumor region. Subsequently, the BEL-7402 tumor-bearing BALB/c nude mice in group 5 received the administration of RT. Finally, The BEL-7402 tumor-bearing mice in group g received the RT administration at 30 min after the exposure of an 808 nm laser. After treatment, mouse weight and tumor volume were measured in the following days using a vernier caliper, and the whole experiment lasted 22 days. The relative tumor volume was calculated with the following formula: relative tumor volume = V/V_0 , where V (mm³) is the volume of the tumor at the day of measurement, and V_0 is the volume of the tumor at the first day in each mouse. After the whole experiment was complete, all BEL-7402 tumor-bearing BALB/c nude mice were sacrificed under protocols approved by the Key Laboratory for Biomedical Effects of Nanomaterials and Nanosafety (Institute of High Energy Physics, CAS).

Blood Hematology and Biochemistry Analysis. Healthy BALB/c female mice were sacrificed under guidelines approved by the Key Laboratory for Biomedical Effects of Nanomaterials and Nanosafety (Institute of High Energy Physics, CAS), and blood samples were collected from the fundus artery after intravenous injection of 200 μ L of PBS and WS₂ QD (20 mg/kg) solution at 1, 3, 6, 9, 15, and 30 days. Approximately 100 μ L of the collected blood sample solution was set in the anticoagulant tube (potassium EDTA collection tube) for hematology analysis. One milliliter of the residual blood was collected from each mouse, set at room temperature for 2 h, and then centrifuged at 1500 rpm for 5 min to remove blood cells. The obtained blood plasma was used for the biochemistry test. The analyses of biochemistry and blood hematology were finished at the animal department of the Peking University medical laboratory.

Pathology Analysis. Healthy BALB/c female mice were sacrificed, and organs of interest from those mice, including heart, liver, spleen, lung, and kidney, were collected at 1 and 30 days after intravenous administration of 200 μ L of PBS and WS₂ QD (20 mg/kg) solution. The organs were set in 4% paraformaldehyde solution for fixing, set in paraffin, and stained with H&E. The slice was examined with an inverted luminescence microscope (OLYMPUS X73, Japan).

Characterization. The morphologies and size of the WS₂ QD samples were characterized by TEM (Tecnai G2 20 S-TWIN). AFM (Agilent 5500, Agilent, USA) was also employed to characterize the size of the WS₂ QD samples. Nicomp380 ZLS plus ZETADi was used to further demonstrate the size distribution and ζ -potential of the as-synthesized WS₂ QD samples. XRD (Japan Rigaku D/max-2500 diffractometer) with Cu K α radiation (λ = 1.54056 Å) was acquired to obtain the crystal phase of the as-synthesized WS₂ QD samples. The UV-vis spectrum of the WS₂ QD samples was recorded on a UV-vis spectrophotometer (U3900, Hitachi). A thermal imaging camera (E40, FLIR) was used to record the temperature curve of the as-synthesized WS₂ QD samples and to take infrared thermal images. A microplate reader (Thermo Multiskan MK3) was used to assess the cell viability assay at an optical absorbance of 450 nm, and an inverted luminescence microscopy (OLYMPUS X73, Japan) was employed to take the luminescence microscopy images.

Conflict of Interest: The authors declare no competing financial interest.

Acknowledgment. This work was supported by the National Basic Research Programs of China (973 programs, Nos.

2012CB932500 and 2015CB932104) and the NSFC (Nos. 21177128, 31751015, and 21320102003).

Supporting Information Available: The Supporting Information is available free of charge on the ACS Publications website at DOI: 10.1021/acsnano.5b05825.

Additional experimental details and figures (PDF)

REFERENCES AND NOTES

- Xiao, Q.; Zheng, X.; Bu, W.; Ge, W.; Zhang, S.; Chen, F.; Xing, H.; Ren, Q.; Fan, W.; Zhao, K.; et al. A Core/Satellite Multifunctional Nanotheranostic for *in Vivo* Imaging and Tumor Eradication by Radiation/Photothermal Synergistic Therapy. *J. Am. Chem. Soc.* **2013**, *135*, 13041–13048.
- Liu, T.; Shi, S.; Cheng, L.; Shen, S.; Cheng, L.; Wang, C.; Song, X.; Goel, S.; Barnhart, T.; Cai, W.; et al. Iron Oxide Decorated MoS₂ Nanosheets with Double PEGylation for Chelator-Free Radiolabeling and Multimodal Imaging Guided Photothermal Therapy. *ACS Nano* **2015**, *9*, 950–960.
- Lv, R.; Yang, P.; He, F.; Gai, S.; Li, C.; Dai, Y.; Yang, G.; Lin, J. A Yolk-like Multifunctional Platform for Multimodal Imaging and Synergistic Therapy Triggered by a Single Near-Infrared Light. *ACS Nano* **2015**, *9*, 1630–1647.
- Mou, J.; Li, P.; Liu, C.; Xu, H.; Song, L.; Wang, J.; Zhang, K.; Chen, Y.; Shi, J.; Chen, H. Ultrasmall Cu₂S Nanodots for Highly Efficient Photoacoustic Imaging-Guided Photothermal Therapy. *Small* **2015**, *11*, 2275–2283.
- Liu, Z.; Cheng, L.; Zhang, L.; Yang, Z.; Liu, Z.; Fang, J. Sub-100 nm Hollow Au-Ag Alloy Urchin-Shaped Nanostructure with Ultrahigh Density of Nanotips for Photothermal Cancer Therapy. *Biomaterials* **2014**, *35*, 4099–4107.
- Liang, C.; Diao, S.; Wang, C.; Gong, H.; Liu, T.; Hong, G.; Shi, X.; Dai, H.; Liu, Z. Tumor Metastasis Inhibition by Imaging-Guided Photothermal Therapy with Single-Walled Carbon Nanotubes. *Adv. Mater.* **2014**, *26*, 5646–5652.
- Cheng, L.; Wang, C.; Feng, L.; Yang, K.; Liu, Z. Functional Nanomaterials for Phototherapies of Cancer. *Chem. Rev.* **2014**, *114*, 10869–10939.
- Wang, C.; Xu, L.; Liang, C.; Xiang, J.; Peng, R.; Liu, Z. Immunological Responses Triggered by Photothermal Therapy with Carbon Nanotubes in Combination with Anti-CTLA-4 Therapy to Inhibit Cancer Metastasis. *Adv. Mater.* **2014**, *26*, 8154–8162.
- Song, X.; Wang, X.; Yu, S.; Cao, J.; Li, S.; Li, J.; Liu, G.; Yang, H.; Chen, X. Co₉Se₈ Nanoplates as A New Theranostic Platform for Photoacoustic/Magnetic Resonance Dual-Modal-Imaging-Guided Chemo-Photothermal Combination Therapy. *Adv. Mater.* **2015**, *27*, 3285–3291.
- Peng, J.; Zhao, L.; Zhu, X.; Sun, Y.; Feng, W.; Gao, Y.; Wang, L.; Li, F. Hollow Silica Nanoparticles Loaded with Hydrophobic Phthalocyanine for Near-Infrared Photodynamic and Photothermal Combination Therapy. *Biomaterials* **2013**, *34*, 7905–7912.
- Cao, W.; Gu, Y.; Meineck, M.; Xu, H. The Combination of Chemotherapy and Radiotherapy Towards More Efficient Drug Delivery. *Chem. - Asian J.* **2014**, *9*, 48–57.
- Tian, B.; Wang, C.; Zhang, S.; Feng, L.; Liu, Z. Photothermally Enhanced Photodynamic Therapy Delivered by Nanographene Oxide. *ACS Nano* **2011**, *5*, 7000–7009.
- Ma, M.; Huang, Y.; Chen, H.; Jia, X.; Wang, S.; Wang, Z.; Shi, J. Bi₂S₃-Embedded Mesoporous Silica Nanoparticles for Efficient Drug Delivery and Interstitial Radiotherapy Sensitization. *Biomaterials* **2015**, *37*, 447–455.
- Huang, Y.; Luo, Y.; Zheng, W.; Chen, T. Rational Design of Cancer-Targeted BSA Protein Nanoparticles as Radiosensitizer to Overcome Cancer Radioresistance. *ACS Appl. Mater. Interfaces* **2014**, *6*, 19217–19228.
- He, L.; Lai, H.; Chen, T. Dual-Function Nanosystem for Synergetic Cancer Chemo-/Radiotherapy Through ROS-Mediated Signaling Pathways. *Biomaterials* **2015**, *51*, 30–42.
- Zhang, X.; Luo, Z.; Chen, J.; Song, S.; Yuan, X.; Shen, X.; Wang, H.; Sun, Y.; Gao, K.; Zhang, L.; et al. Ultrasmall Glutathione-protected Gold Nanoclusters as Next Generation

- Radiotherapy Sensitizers with High Tumor Uptake and High Renal Clearance. *Sci. Rep.* **2015**, *5*, 8669.
17. Zhang, X.; Luo, Z.; Chen, J.; Shen, X.; Song, S.; Sun, Y.; Fan, S.; Fan, F.; Leong, D.; Xie, J. Ultrasmall Au_{10–12}(SG)_{10–12} Nanomolecules for High tumor Specificity and Cancer Radiotherapy. *Adv. Mater.* **2014**, *26*, 4565–4568.
 18. Ma, N.; Xu, H.; An, L.; Li, J.; Sun, Z.; Zhang, X. Radiation-sensitive Diselenide Block Co-polymer Micellar Aggregates: Toward the Combination of Radiotherapy and Chemotherapy. *Langmuir* **2011**, *27*, 5874–5878.
 19. Hainfeld, J.; Lin, L.; Slatkin, D.; Avraham Dilmanian, F.; Vadas, T.; Smilowitz, H. Gold Nanoparticle Hyperthermia Reduces Radiotherapy Dose. *Nanomedicine* **2014**, *10*, 1609–1617.
 20. Liu, Y.; Liu, Y.; Bu, W.; Xiao, Q.; Sun, Y.; Zhao, K.; Fan, W.; Liu, J.; Shi, J. Radiation-/Hypoxia-Induced Solid Tumor Metastasis and Regrowth Inhibited by Hypoxia-Specific Upconversion Nanoradiosensitizer. *Biomaterials* **2015**, *49*, 1–8.
 21. Fan, W.; Shen, B.; Bu, W.; Chen, F.; He, Q.; Zhao, K.; Zhang, S.; Zhou, L.; Peng, W.; Xiao, Q.; et al. A Smart Upconversion-Based Mesoporous Silica Nanotheranostic System for Synergetic Chemo-/Radio-/Photodynamic Therapy and Simultaneous MR/UCL Imaging. *Biomaterials* **2014**, *35*, 8992–9002.
 22. Chen, L.; Zhong, X.; Yi, X.; Huang, M.; Ning, P.; Liu, T.; Ge, C.; Chai, Z.; Liu, Z.; Yang, K. Radionuclide ¹³¹I Labeled Reduced Graphene Oxide for Nuclear Imaging Guided Combined Radio- and Photothermal Therapy of Cancer. *Biomaterials* **2015**, *66*, 21–28.
 23. Zhang, Z.; Wang, J.; Chen, C. Near-Infrared Light-Mediated Nanoplatforams for Cancer Thermo-Chemotherapy and Optical Imaging. *Adv. Mater.* **2013**, *25*, 3869–3880.
 24. Wang, S.; Huang, P.; Nie, L.; Xing, R.; Liu, D.; Wang, Z.; Lin, J.; Chen, S.; Niu, G.; Lu, G.; et al. Single Continuous Wave Laser Induced Photodynamic/Plasmonic Photothermal Therapy Using Photosensitizer-Functionalized Gold Nanostars. *Adv. Mater.* **2013**, *25*, 3055–3061.
 25. Su, Y.; Wei, X.; Peng, F.; Zhong, Y.; Lu, Y.; Su, S.; Xu, T.; Lee, S.; He, Y. Gold Nanoparticles-Decorated Silicon Nanowires as Highly Efficient Near-Infrared Hyperthermia Agents for Cancer Cells Destruction. *Nano Lett.* **2012**, *12*, 1845–1850.
 26. Gao, L.; Fei, J.; Zhao, J.; Li, H.; Cui, Y.; Li, J. Hypocrellin-Loaded Gold Nanocages with High Two-Photon Efficiency for Photothermal/Photodynamic Cancer Therapy *in Vitro*. *ACS Nano* **2012**, *6*, 8030–8040.
 27. Fan, Z.; Dai, X.; Lu, Y.; Yu, E.; Brahmabatt, N.; Carter, N.; Tchouwou, C.; Singh, A.; Jones, Y.; Yu, H.; et al. Enhancing Targeted Tumor Treatment by Near IR Light-Activatable Photodynamic-Photothermal Synergistic Therapy. *Mol. Pharmaceutics* **2014**, *11*, 1109–1116.
 28. Jang, B.; Park, J.; Tung, C.; Kim, I.; Choi, Y. Gold Nanorod-Photosensitizer Complex for Near-Infrared Fluorescence Imaging and Photodynamic/Photothermal Therapy *In Vivo*. *ACS Nano* **2011**, *5*, 1086–1094.
 29. Zhou, M.; Zhang, R.; Huang, M.; Lu, W.; Song, S.; Melancon, M.; Tian, M.; Liang, D.; Li, C. A Chelator-free Multifunctional [⁶⁴Cu]-CuS Nanoparticle Platform for Simultaneous Micro-PET/CT Imaging and Photothermal Ablation Therapy. *J. Am. Chem. Soc.* **2010**, *132*, 15351–15358.
 30. Zha, Z.; Wang, S.; Zhang, S.; Qu, E.; Ke, H.; Wang, J.; Dai, Z. Targeted Delivery of CuS Nanoparticles Through Ultrasound Image-Guided Microbubble Destruction for Efficient Photothermal Therapy. *Nanoscale* **2013**, *5*, 3216–3219.
 31. Tian, Q.; Tang, M.; Sun, Y.; Zou, R.; Chen, Z.; Zhu, M.; Yang, S.; Wang, J.; Wang, J.; Hu, J. Hydrophilic Flower-Like CuS Superstructures as An Efficient 980 nm Laser-Driven Photothermal Agent for Ablation of Cancer Cells. *Adv. Mater.* **2011**, *23*, 3542–3547.
 32. Tian, Q.; Jiang, F.; Zou, R.; Liu, Q.; Chen, Z.; Zhu, M.; Yang, S.; Wang, J.; Wang, J.; Hu, J. Hydrophilic Cu₂S Nanocrystals: A Photothermal Agent with a 25.7% Heat Conversion Efficiency for Photothermal Ablation of Cancer Cells *in Vivo*. *ACS Nano* **2011**, *5*, 9761–9771.
 33. Ku, G.; Zhou, M.; Song, S.; Huang, Q.; Hazle, J.; Li, C. Copper Sulfide Nanoparticles As a New Class of Photoacoustic Contrast Agent for Deep Tissue Imaging at 1064 nm. *ACS Nano* **2012**, *6*, 7489–7496.
 34. Song, G.; Han, L.; Zou, W.; Xiao, Z.; Huang, X.; Qin, Z.; Zou, R. A Novel Photothermal Nanocrystals of Cu₂S₄ Hollow Structure for Efficient Ablation of Cancer Cells. *Nano-Micro Lett.* **2014**, *6*, 169–177.
 35. Wang, S.; Li, X.; Chen, Y.; Cai, X.; Yao, H.; Gao, W.; Zheng, Y.; An, X.; Shi, J.; Chen, H. A Facile One-Pot Synthesis of a Two-Dimensional MoS₂/Bi₂S₃ Composite Theranostic Nanosystem for Multi-Modality Tumor Imaging and Therapy. *Adv. Mater.* **2015**, *27*, 2775–2782.
 36. Liu, J.; Zheng, X.; Yan, L.; Zhou, L.; Tian, G.; Yin, W.; Wang, L.; Liu, Y.; Hu, Z.; Gu, Z.; et al. Bismuth Sulfide Nanorods as a Precision Nanomedicine for *in Vivo* Multimodal Imaging-Guided Photothermal Therapy of Tumor. *ACS Nano* **2015**, *9*, 696–707.
 37. Li, J.; Jiang, F.; Yang, B.; Song, X.; Liu, Y.; Yang, H.; Cao, D.; Shi, W. R.; Chen, G. Topological Insulator Bismuth Selenide as a Theranostic Platform for Simultaneous Cancer Imaging and Therapy. *Sci. Rep.* **2013**, *3*, 1998.
 38. Song, G.; Liang, C.; Gong, H.; Li, M.; Zheng, X.; Cheng, L.; Yang, K.; Jiang, X.; Liu, Z. Core-Shell MnSe@Bi₂Se₃ Fabricated via a Cation Exchange Method as Novel Nanotheranostics for Multimodal Imaging and Synergistic Theranoradiotherapy. *Adv. Mater.* **2015**, *27*, 6110.
 39. Liu, Z.; Sun, X.; Nakayama-Ratchford, N.; Dai, H. Supramolecular Chemistry on Water-Soluble Carbon Nanotubes for Drug Loading and Delivery. *ACS Nano* **2007**, *1*, 50–56.
 40. Liu, Z.; Robinson, J.; Sun, X.; Dai, H. PEGylated Nanographene Oxide for Delivery of Water-Insoluble Cancer Drugs. *J. Am. Chem. Soc.* **2008**, *130*, 10876–10877.
 41. Zhu, Z.; Tang, Z.; Phillips, J.; Yang, R.; Wang, H.; Tan, W. Regulation of Singlet Oxygen Generation Using Single-Walled Carbon Nanotubes. *J. Am. Chem. Soc.* **2008**, *130*, 10856–10857.
 42. Wu, H.; Liu, G.; Wang, X.; Zhang, J.; Chen, Y.; Shi, J.; Yang, H.; Hu, H.; Yang, S. Solvothermal Synthesis of Cobalt Ferrite Nanoparticles Loaded on Multiwalled Carbon Nanotubes for Magnetic Resonance Imaging and Drug Delivery. *Acta Biomater.* **2011**, *7*, 3496–3504.
 43. Wang, X.; Wang, C.; Cheng, L.; Lee, S.; Liu, Z. Noble Metal Coated Single-Walled Carbon Nanotubes for Applications in Surface Enhanced Raman Scattering Imaging and Photothermal Therapy. *J. Am. Chem. Soc.* **2012**, *134*, 7414–7422.
 44. Liu, Z.; Robinson, J.; Tabakman, S.; Yang, K.; Dai, H. Carbon Materials for Drug Delivery & Cancer Therapy. *Mater. Today* **2011**, *14*, 316–323.
 45. Liu, Z.; Chen, K.; Davis, C.; Sherlock, S.; Cao, Q.; Chen, X.; Dai, H. Drug Delivery with Carbon Nanotubes for *in Vivo* Cancer Treatment. *Cancer Res.* **2008**, *68*, 6652–6660.
 46. Liu, X.; Tao, H.; Yang, K.; Zhang, S.; Lee, S.; Liu, Z. Optimization of Surface Chemistry on Single-Walled Carbon Nanotubes for *in Vivo* Photothermal Ablation of Tumors. *Biomaterials* **2011**, *32*, 144–151.
 47. Huang, P.; Lin, J.; Wang, X.; Wang, Z.; Zhang, C.; He, M.; Wang, K.; Chen, F.; Li, Z.; Shen, G.; et al. Light-Triggered Theranostics Based on Photosensitizer-Conjugated Carbon Dots for Simultaneous Enhanced-Fluorescence Imaging and Photodynamic Therapy. *Adv. Mater.* **2012**, *24*, 5104–5110.
 48. Chen, D.; Wang, C.; Nie, X.; Li, S.; Li, R.; Guan, M.; Liu, Z.; Chen, C.; Wang, C.; Shu, C.; et al. Photoacoustic Imaging Guided Near-Infrared Photothermal Therapy Using Highly Water-Dispersible Single-Walled Carbon Nanohorns as Theranostic Agents. *Adv. Funct. Mater.* **2014**, *24*, 6621–6628.
 49. Wang, C.; Cheng, L.; Liu, Z. Upconversion Nanoparticles for Photodynamic Therapy and Other Cancer Therapeutics. *Theranostics* **2013**, *3*, 317–330.
 50. Fan, W.; Shen, B.; Bu, W.; Zheng, X.; He, Q.; Cui, Z.; Zhao, K.; Zhang, S.; Shi, J. Design of an Intelligent Sub-50 nm Nuclear-Targeting Nanotheranostic System for Imaging Guided Intracranial Radiosensitization. *Chem. Sci.* **2015**, *6*, 1747–1753.

51. Fan, W.; Bu, W.; Zhang, Z.; Shen, B.; Zhang, H.; He, Q.; Ni, D.; Cui, Z.; Zhao, K.; Bu, J.; et al. X-ray Radiation-Controlled NO-Release for On-Demand Depth-Independent Hypoxic Radiosensitization. *Angew. Chem.* **2015**, 10.1002/ange.201504536.
52. Chen, Q.; Wang, C.; Cheng, L.; He, W.; Cheng, Z.; Liu, Z. Protein Modified Upconversion Nanoparticles for Imaging-Guided Combined Photothermal and Photodynamic Therapy. *Biomaterials* **2014**, 35, 2915–2923.
53. Cao, T.; Yang, Y.; Sun, Y.; Wu, Y.; Gao, Y.; Feng, W.; Li, F. Biodistribution of Sub-10 nm PEG-Modified Radioactive/Upconversion Nanoparticles. *Biomaterials* **2013**, 34, 7127–7134.
54. Wu, X.; Chen, G.; Shen, J.; Li, Z.; Zhang, Y.; Han, G. Upconversion Nanoparticles: A Versatile Solution to Multi-scale Biological Imaging. *Bioconjugate Chem.* **2015**, 26, 166–175.
55. Punjabi, A.; Wu, X.; Tokatli-Apollon, A.; El-Rifai, M.; Lee, H.; Zhang, Y.; Wang, C.; Liu, Z.; Chan, E. M.; Duan, C.; et al. Amplifying the Red-Emission of Upconverting Nanoparticles for Biocompatible Clinically Used Prodrug-Induced Photodynamic Therapy. *ACS Nano* **2014**, 8, 10621–10630.
56. Li, Z.; Zhang, Y.; Wu, X.; Huang, L.; Li, D.; Fan, W.; Han, G. Direct Aqueous-Phase Synthesis of Sub-10 nm “Luminous Pearls” with Enhanced *in Vivo* Renewable Near-Infrared Persistent Luminescence. *J. Am. Chem. Soc.* **2015**, 137, 5304–5307.
57. Yin, W.; Yan, L.; Yu, J.; Tian, G.; Zhou, L.; Zheng, X.; Zhang, X.; Yong, Y.; Li, J.; Gu, Z.; et al. High-Throughput Synthesis of Single-Layer MoS₂ Nanosheets as a Near-Infrared Photothermal-Triggered Drug Delivery for Effective Cancer Therapy. *ACS Nano* **2014**, 8, 6922–6933.
58. Wang, S.; Li, K.; Chen, Y.; Chen, H.; Ma, M.; Feng, J.; Zhao, Q.; Shi, J. Biocompatible PEGylated MoS₂ Nanosheets: Controllable Bottom-up Synthesis and Highly Efficient Photothermal Regression of Tumor. *Biomaterials* **2015**, 39, 206–217.
59. Liu, T.; Wang, C.; Gu, X.; Gong, H.; Cheng, L.; Shi, X.; Feng, L.; Sun, B.; Liu, Z. Drug Delivery with PEGylated MoS₂ Nanosheets for Combined Photothermal and Chemotherapy of Cancer. *Adv. Mater.* **2014**, 26, 3433–3440.
60. Liu, T.; Wang, C.; Cui, W.; Gong, H.; Liang, C.; Shi, X.; Li, Z.; Sun, B.; Liu, Z. Combined Photothermal and Photodynamic Therapy Delivered by PEGylated MoS₂ Nanosheets. *Nanoscale* **2014**, 6, 11219–11225.
61. Chou, S.; Kaehr, B.; Kim, J.; Foley, B.; De, M.; Hopkins, P.; Huang, J.; Brinker, C.; Dravid, V. Chemically Exfoliated MoS₂ as Near-Infrared Photothermal Agents. *Angew. Chem., Int. Ed.* **2013**, 52, 4160–4164.
62. Yong, Y.; Zhou, L.; Gu, Z.; Yan, L.; Tian, G.; Zheng, X.; Liu, X.; Zhang, X.; Shi, J.; Cong, W.; et al. WS₂ Nanosheet as a New Photosensitizer Carrier for Combined Photodynamic and Photothermal Therapy of Cancer Cells. *Nanoscale* **2014**, 6, 10394–10403.
63. Yang, G.; Gong, H.; Liu, T.; Sun, X.; Cheng, L.; Liu, Z. Two-Dimensional Magnetic WS₂@Fe₃O₄ Nanocomposite with Mesoporous Silica Coating for Drug Delivery and Imaging-Guided Therapy of Cancer. *Biomaterials* **2015**, 60, 62–71.
64. Tan, C.; Zhang, H. Two-Dimensional Transition Metal Dichalcogenide Nanosheet-Based Composites. *Chem. Soc. Rev.* **2015**, 44, 2713–2731.
65. Cheng, L.; Liu, J.; Gu, X.; Gong, H.; Shi, X.; Liu, T.; Wang, C.; Wang, X.; Liu, G.; Xing, H.; et al. PEGylated WS₂ Nanosheets as a Multifunctional Theranostic Agent for *in Vivo* Dual-Modal CT/Photoacoustic Imaging Guided Photothermal Therapy. *Adv. Mater.* **2014**, 26, 1886–1893.
66. Chen, Y.; Tan, C.; Zhang, H.; Wang, L. Two-Dimensional Graphene Analogues for Biomedical Applications. *Chem. Soc. Rev.* **2015**, 44, 2681–2701.
67. Lin, L.; Xu, Y.; Zhang, S.; Ross, I.; Ong, A.; Allwood, D. Fabrication of Luminescent Monolayered Tungsten Dichalcogenides Quantum Dots with Giant Spin-Valley Coupling. *ACS Nano* **2013**, 7, 8214–8223.
68. Sun, Y.; Sun, Z.; Gao, S.; Cheng, H.; Liu, Q.; Lei, F.; Wei, S.; Xie, Y. All-Surface-Atomic-Metal Chalcogenide Sheets for High-Efficiency Visible-Light Photoelectrochemical Water Splitting. *Adv. Energy Mater.* **2014**, 4, 1300611.
69. Guo, C.; Dong, Y.; Yang, H.; Li, C. Graphene Quantum Dots as a Green Sensitizer to Functionalize ZnO Nanowire Arrays on F-Doped SnO₂ Glass for Enhanced Photoelectrochemical Water Splitting. *Adv. Energy Mater.* **2013**, 3, 997–1003.
70. Zhou, Z.; Kong, B.; Yu, C.; Shi, X.; Wang, M.; Liu, W.; Sun, Y.; Zhang, Y.; Yang, H.; Yang, S. Tungsten Oxide Nanorods: An Efficient Nanoplatfor for Tumor CT Imaging and Photothermal Therapy. *Sci. Rep.* **2014**, 4, 3653.